A method to produce and validate a digitally reconstructed radiograph-based computer simulation for optimisation of chest radiographs acquired with a computed radiography imaging system

[1,2]C S MOORE, BSc, MSc, [1]G P LINEY, BSc, PhD, [1,3,4]A W BEAVIS, BSc, PhD and [1,3]J R SAUNDERSON, BSc, MSc

[1]*Radiation Physics Department, Queen's Centre for Oncology and Haematology, Castle Hill Hospital, Hull & East Yorkshire Hospitals, Castle Road, Hull, UK,* [2]*Department of Computer Science, Faculty of Science, University of Hull, Cottingham Road, Hull, UK,* [3]*Postgraduate Medical Institute, University of Hull, Kingston Upon Hull, UK, and* [4]*Faculty of Health and Wellbeing, Sheffield Hallam University, City Campus, Howard Street, Sheffield, UK*

Objectives: The purpose of this study was to develop and validate a computer model to produce realistic simulated computed radiography (CR) chest images using CT data sets of real patients.

Methods: Anatomical noise, which is the limiting factor in determining pathology in chest radiography, is realistically simulated by the CT data, and frequency-dependent noise has been added post-digitally reconstructed radiograph (DRR) generation to simulate exposure reduction. Realistic scatter and scatter fractions were measured in images of a chest phantom acquired on the CR system simulated by the computer model and added post-DRR calculation.

Results: The model has been validated with a phantom and patients and shown to provide predictions of signal-to-noise ratios (SNRs), tissue-to-rib ratios (TRRs: a measure of soft tissue pixel value to that of rib) and pixel value histograms that lie within the range of values measured with patients and the phantom. The maximum difference in measured SNR to that calculated was 10%. TRR values differed by a maximum of 1.3%.

Conclusion: Experienced image evaluators have responded positively to the DRR images, are satisfied they contain adequate anatomical features and have deemed them clinically acceptable. Therefore, the computer model can be used by image evaluators to grade chest images presented at different tube potentials and doses in order to optimise image quality and patient dose for clinical CR chest radiographs without the need for repeat patient exposures.

Many publications [1–5] have shown that patient anatomy is the limiting factor in the detection of lesions in the chest, and the term "anatomical noise" was born out of their work. Recently, a European wide study (the RADIUS chest trial) examined various aspects of nodule detection in digital chest radiology, such as the effects of nodule location and system noise [6, 7], anatomical noise and part of the image background acting as pure noise [8, 9]. In the introductory paper, Bath et al [10] described how projected anatomy in chest radiographs affect pathological detection to a much larger extent than that of system noise, and as such is the limiting factor for the detection of lesions in chest radiographs. Since chest radiography is now generally considered not to be limited by quantum noise, images used to optimise any digital X-ray system for chest radiography must contain clinically realistic features. Typically, work reported in the literature examining computed radiography (CR)

chest optimisation has used physical phantoms which enable optimisation of individual parameters such as signal to noise ratios (SNRs) and modulation transfer function (MTF), but these do not necessarily contain all the anatomical features (noise) required [11–15]. Indeed, we have investigated optimising a CR imaging system for chest radiography with a phantom containing little anatomical detail [16–18] and were able to advise on maximising contrast and spatial resolution, but how those related to the diagnostic quality of the clinical image was undetermined. More recently, computerised voxel phantoms have been used in Monte Carlo studies [19–23] in an attempt to model anatomical features. However, the organs of the voxel phantom used in these studies [24] are identified with only one of five tissue types, namely soft tissue, bone, bone marrow, lung tissue and air, possibly limiting the contribution of anatomical noise, and the resolution of this voxel phantom is relatively coarse (approx 4 mm long × 3 mm wide × 3 mm thick). It is therefore likely to produce images of much lower spatial resolution than a real CR image (typical pixel pitch 0.17 × 0.17 mm). Another consideration is that all of the Monte Carlo studies

Address correspondence to: Mr Craig Moore, Radiation Physics Department, Queen's Centre for Oncology and Haematology, Castle Hill Hospital, Hull & East Yorkshire Hospitals, Castle Road, Hull, HU16 5JQ, UK. E-mail: craig.moore@hey.nhs.uk

calculate energy imparted to the CR storage phosphor only, and do not include system noise.

As discussed, although anatomy is the most important factor in detecting lesions in a digital chest radiograph, the radiation dose–image quality relationship must not be ignored from a governance perspective. The necessity to keep doses as low as reasonably practicable (ALARP) is a recommendation by the International Commission on Radiological Protection (ICRP) [25] and is a requirement in UK law under the Ionising Radiation (Medical Exposure) Regulations 2000 (IR(ME)R 2000). For every examination, doses to the patient must be kept ALARP while obtaining the necessary level of image quality. Bath et al [26] have suggested that clinical images should be used to obtain the highest validity for optimisation, and as such have described a method to simulate lower exposures by adding frequency-dependent noise to an original image [27]. This methodology only works for a given X-ray beam quality, so full optimisation would still necessitate repeat exposures of the same patient, thus increasing the stochastic risk of inducing cancers.

Anatomical and system noise must feature in an image to enable optimisation (as has been demonstrated in the literature). This paper describes the development and validation of a digitally reconstructed radiograph (DRR): a computer simulation of a conventional two-dimensional (2D) X-ray image created from CT data. Our model includes realistic anatomical and frequency-dependent system noise (including quantum noise) for the purpose of optimising CR chest radiographs of average size males. The model uses clinical chest CT data sets to provide realistic anatomical features. To our knowledge, DRR-generated images have not been used for optimisation purposes. In our new model, a ray-casting method of DRR generation was used, as this method has been proven to produce superior quality in the resultant images [28, 29] than those produced by other methods such as splatting [30] (a method which projects each voxel to the image plane and composites it into an accumulated image). The X-ray spectra used in the simulation are generated by the Institute of Physics and Engineering in Medicine (IPEM) Report 78 software [31]. Energy absorbed in the CR storage phosphor, scatter and frequency-dependent noise are modelled according to physical characteristics of the CR system. As resulting images are computer generated using retrospective CT data sets, no extra exposure risk to patients exists.

Methods and materials

Practical methodology

The DRR simulation requires data derived from a CR and CT system to enable adequate functionality. All physical characteristics required of the X-ray and CR system were measured in a general purpose X-ray room equipped with a Philips Optimus Diagnost TH (Philips Medical Systems, Surrey, UK) ceiling-suspended X-ray system with total inherent filtration equivalent to 3.1 mm of aluminium, and using an Agfa CR-85 reader with MD4.0 plates (Agfa, Peissenberg, Germany) (35 × 43 cm, effective pixel pitch of 0.17 mm). All phantom

acquisitions (CR and CT) utilised the chest portion of the Alderson RANDO anthropomorphic phantom, consisting of a natural human skeleton embedded in a synthetic isocyanate rubber with lung substitute and air cavities, simulating the average male, approximately 70 kg. Although primarily used for radiation therapy, RANDO has been shown to attenuate diagnostic energy radiation similar to that of water, which in turn has very similar properties to human muscle [32]. All phantom images acquired on the CR system (at each tube potential) were made with a focus to receptor distance of 180 cm with the CR receptor placed 5 cm behind the phantom in the cassette holder, and sufficient tube current–time product (mAs) to produce a lgM value of 2.00 ± 0.05. The lgM value is a receptor dose indicator displayed on the CR system for every image acquisition, which Agfa recommends should be approximately 2.00 for a correctly exposed chest radiograph. The X-ray field was collimated to the edges of the phantom and since different individual receptors do not have exactly matching sensitivities, a single CR cassette (digitised in the CR reader with a fixed sensitivity of 400) was used throughout the study. The cassette chosen demonstrated a median sensitivity (*i.e.* a median lgM value compared with the other cassettes). No clinical post-processing was applied. A Philips 16 slice multidetector CT scanner was used to collect CT phantom and patient data. It has been reported recently by Roberts et al [33] that the use of antiscatter grids with digital imaging is not justified because of the resulting increase in patient dose without a corresponding increase in image quality. In accordance with this, and the chest imaging protocol in our radiology department, an antiscatter grid was not modelled in our simulation.

Computer model

X-ray spectra

X-ray spectra were generated using the techniques of Birch and Marshall as described in IPEM Report 78 [31]. The report generates spectra at 0.5 keV intervals from 0.5 keV up to the accelerating potential chosen by the user. The spectral data is specified on a central axis 750 mm from the source (photons mm^{-2} mAs^{-1}). As the beam originates from a point source, the fluence used in the simulator was corrected using the inverse square law depending on the distance from the source to the virtual patient. IPEM Report 78 calculates X-ray spectra for tubes that are 100% efficient so the fluence was also scaled to the measured air kerma of the X-ray tube used in this work.

CT data preparation

Prior to DRR calculation, it was necessary to prepare the CT data. CT images should have as little processing applied as possible, so that pixel values (CT numbers) correspond to the X-ray attenuation properties of the particular tissue. As back-projected CT data are inherently blurred, filtering must be applied. The Philips scanner used in this study has a variety of filters, some of which artificially sharpen the image (emphasise high spatial frequencies), some of which smooth the image (emphasise low frequencies). After discussion with

Philips (Paul Klahr, personal communication, Philips Medical Systems, 2008), filter (E) was identified as providing minimum processing. This is the basic ''ramp'' filter that corrects the effect back-projection has on the amplitudes of different spatial frequencies in the image. On the scanner, CT data can be reconstructed with filter (E) by reprocessing the raw data. The field of view (FOV) and reconstruction matrix can also be altered, although the FOV is somewhat dependent on patient size.

It is well understood that CT images contain noise due to a number of sources, primarily electronic, quantum and reconstruction filter. Typically, noise in CT images is Gaussian and independent of tissue attenuation, as discussed by Hilts and Duzenli [34]. To assess whether this noise has any affect on the final characteristics of a DRR image, a Gaussian noise-removing filter (mean adaptive filter) with varying kernel sizes of 0×0 (*i.e.* no filter applied), 7×7, 14×14 and 21×21 was applied to the CT data prior to DRR calculation (see below). Frequency-dependent noise (see below) was added to the raw DRRs, and signal to noise ratio (SNR) and dynamic range comparisons were made. CT images also exhibit scattered radiation to some extent, but the scanner used in this study utilises post-patient collimation that minimises scatter detected (nominally only 1–2% of the signal is due to scatter) so no correction for this was deemed necessary.

CT number to linear attenuation coefficient conversion

The ray-casting DRR method requires each CT number to be converted to its linear attenuation coefficient (LAC) in order that one may calculate the outgoing photon intensity from knowledge of the incoming photon intensity. The Gammex RMI radiotherapy tissue equivalent phantom (model no. 467) (Gammex RMI, Nottingham, UK) is a solid water cylinder that contains 17 inserts, the attenuation properties of which mimic the range of attenuations of the various tissues found *in vivo*, as shown in Figure 1. This phantom was scanned using the parameters described in Table 1. These parameters are standard for chest imaging in our radiology CT department (tube current is typical for those of average sized males). After the scan, raw data were reconstructed with filter (E), matrix 1024 and slice thickness 0.8 mm (the same reconstruction parameters to be used to prepare clinical images for DRR calculation). The images were transferred to a separate computer for analysis and the mean CT number of each tissue substitute was derived. We have assumed that beam hardening has minimal impact on the results, as the CT scanner utilises a ''bow-tie'' filter to conform the shape of the beam to the body, and scanner software corrects for any further artefact. Information from the user manual of the RMI phantom provides the elemental composition of each tissue substitute by weight (*e.g.* composition of lung by percentage weight is H=8.33, C=60.32, N=1.67, O=17.38, Cl=0.15, Si=0.61 and Mg=11.54). These data were entered into the XCOM database [35] together with an X-ray spectrum produced by IPEM 78. The database calculates total attenuation ($cm^2 g^{-1}$) for each energy in the spectrum, and assuming one knows the density ($g cm^{-3}$) of the substitute it is simple to convert to
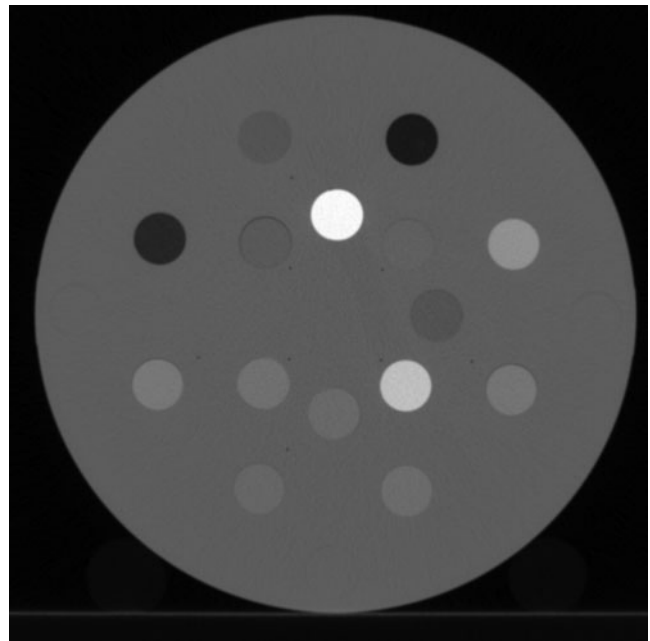

Figure 1. Gammex RMI tissue substitute phantom with each insert visible.

LAC (cm^{-1}). To illustrate this point, Table 2 shows the first five energies of a 50 kVp spectrum together with total attenuation and LACs for the lung substitute (it should be noted that the XCOM database gives a maximum 10% error on the attenuation values). This process was repeated for all tissue substitutes with all virtual tube potentials used for this study (50–150 kVp in steps of 10). Table 3 shows the first 3 energies of the 50 kVp spectrum with LACs for each substitute. Data from Table 3 can then be used to derive linear relationships between mean CT numbers and LACs. For example, there is a linear relationship (r^2=0.997) between CT number and LACs from air (CT=21) to LN450 (CT=443). The resulting linear equation is used to convert those voxels in the CT data that range from 21 to 443 (all CT numbers lower than 21 were converted to 21) to their respective LACs. Moving down the table the next linear relationship that exists with a high degree of correlation (r^2=1) is LN450 (443) to adipose (909). As such, all voxel values that lie in the range 443–909 were converted to their relevant LACs depending on the linear relationship. This process was continued until all CT voxel values were transformed to their respective LAC. Very few CT voxel values existed above 2516 (cortical bone), but those that did were converted using the linear relationship for CB2-30% to cortical bone (*i.e.* the final linear relationship derived from Table 3).

Table 1. Scan parameters used to scan the Gammex RMI phantom

CT scan parameter	Value used
Resolution	Standard
Collimation	16×0.75 mm
Pitch	1
FOV (mm)	350
Tube potential (kVp)	120
Tube current–time product (mAs)	175

FOV, field of view.

Table 2. First five photon energies in a virtual 50 kVp spectrum together with their respective total attenuation and linear attenuation coefficient

Photon energy (keV)	Total attenuation (cm^2 g^{-1})	Linear attenuation coefficient (cm^{-1})
13.0	2.49	0.747
13.5	2.24	0.672
14.0	2.03	0.609
14.5	1.84	0.552
15.0	1.68	0.504

DRR calculation

The DRR calculations were made using a ray-casting method by summing CT attenuation data along a pencil beam from the simulated X-ray source to each pixel in the resultant image. Figure 2 shows a pencil beam entering a voxel in the first slice of the 3D CT data set. Each voxel is $0.8 \times 0.34 \times 0.34$ mm in size (height × width × depth), because the CT data were flipped to a posteroanterior (PA) orientation (simulating the patient in an erect position). As such, each voxel height, width and depth is the same dimension as the CT slice thickness, and CT pixel resolution in x and y respectively. One pencil beam per "first PA slice voxel" (Figure 2 shows only one beam) was used in the model, and each is the size of a voxel. There is very little increase in size of each pencil beam as it moves through the CT data set (mean increase of 7%), so no correction was applied for this. The projection function uses a 1:1 mapping between pixels on the DRR and voxels on the front face (first PA slice) of the CT data set, resulting in a simulated image with a pixel density 700 rows × 1024 columns (*i.e.* no. of CT slices × CT resolution), and resolution of 0.8×0.34 mm. This is smaller than a CR image (2800 × 2300, pixel pitch 0.17×0.17 mm), but is discussed under "Energy absorbed in CR phosphor". The fluence of X-ray photons impinging the face of each voxel in the CT data set as well as the entrance angles of elevation (ϕ) and longitude (θ) are calculated. We have assumed the central axis of each pencil beam impinges the centre of the voxel in the first PA CT slice. As such, no portion of the beam enters neighbouring voxels. However, this is not the case for subsequent PA slices. For example, Figure 3 shows the front face of nine voxels together with a pencil beam impinging the central voxel. Notice that the central axis of the beam does not impinge the centre of the central voxel. The dark square in Figure 3 represents the area of pencil beam impinging not only the voxel in which the central axis impinges, but also the neighbouring voxels. The respective areas of beam in the incident, bottom (or top), right (or left), and corner voxels are calculated and found as a ratio of the whole beam area (RATIO_AREA). The effective LAC is then found by weighting the LAC of the relevant voxel to the RATIO_AREA of beam in the voxel, and summing them together:

$$\begin{aligned} \mathrm{LAC}_{\mathrm{eff}} = &(\mathrm{RATIO\_AREA}_{\mathrm{incident}} \times \mathrm{LAC}_{\mathrm{incident}}) + \\ &(\mathrm{RATIO\_AREA}_{\mathrm{right}} \times \mathrm{LAC}_{\mathrm{right}}) + \\ &(\mathrm{RATIO\_AREA}_{\mathrm{bottom}} \times \mathrm{LAC}_{\mathrm{bottom}}) + \\ &(\mathrm{RATIO\_AREA}_{\mathrm{corner}} \times \mathrm{LAC}_{\mathrm{corner}}) \end{aligned} \tag{1}$$

This is performed in each PA slice in the CT data set until the pencil beam exits. We have used area to correct for partial voxel sampling, which assumes using an area ratio to represent a volume ratio. However, as ray casting is a perspective projection, this assumption is not entirely accurate, since this is a method of mapping 3D (volumetric) points to a two-dimensional plane. Nevertheless, for a given increase/decrease in area of beam in a voxel, the volume of beam in a voxel would approximately increase/decrease proportionally. Using area ratios is for calculation of weighted linear attenuation coefficients only, and as this applies to the whole 3D pencil beam, one is not moving away from a volumetric calculation and as such this method is valid. Other ray-casting methods, such as that described by Siddon [36], simply use rays (rather than pencil beams) to calculate the path of a radiological beam through CT data. Voxel density is weighted to the length of ray in each voxel. In reality, fluence of X-ray photons impinging on voxelated arrays are not simply rays, rather beams that diverge through the

Table 3. First three energies of a virtual 50 kVp spectrum together with the linear attenuation coefficient (LAC) and mean PV of each tissue substitute

| Tissue substitute	Mean CT number	13 keV LAC (cm^{-1})	13.5 keV LAC (cm^{-1})	14 keV LAC (cm^{-1})
Air	21	0.000289	0.00026	0.000235
LN300	282	0.0747	0.0672	0.0609
LN450	443	0.11205	0.1008	0.09135
AP6, adipose	909	0.13708	0.1242	0.11316
Polyethylene	911	0.09568	0.087492	0.080224
Breast	970	0.18216	0.16434	0.14949
CT solid water	1016	0.153	0.13872	0.12648
CB3 resin	1027	0.230945	0.207955	0.1881
Brain	1029	0.159355	0.14413	0.130935
Liver	1113	0.17135	0.1541	0.1403
IB1, inner bone	1114	0.29268	0.26244	0.2376
B200, bone mineral	1143	0.1888	0.1711	0.15576
CB4 resin	1228	0.3744	0.33813	0.30537
CB2-10% (CaCO$_3$)	1301	0.5544	0.4984	0.45024
Acryilc	1329	1.06485	0.958365	0.864475
CB2-30% (CaCO$_3$)	1571	0.90852	0.8174	0.73834
CB2-50% (CaCO$_3$)	2034	1.6224	1.45704	1.31508
SB3, cortical bone	2516	2.484	2.2448	2.024
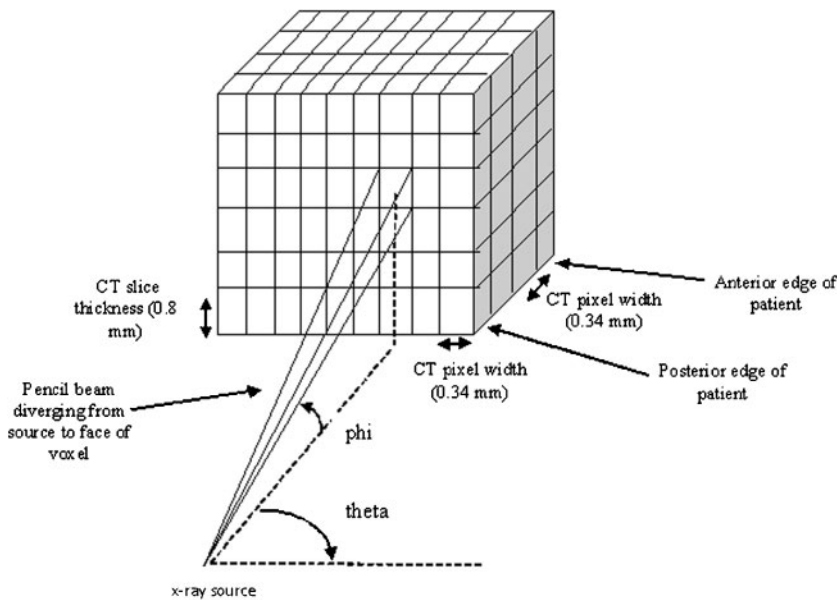
Figure 2. Pencil beam entering a voxel in the first posteroanterior (PA) slice of the CT data set.

array. As such, Siddon's and other techniques using rays are prone to aliasing in the final DRR [37].

The intensity of X-ray photons exiting is calculated with the following formula:

$$
I = I_0 \exp\big(-pathlength \\
\times \big[LAC_{eff\_slice1} + LAC_{eff\_slice2} \ldots\ldots + LAC_{eff\_sliceN} \big] \big) \quad (2)
$$

where I_0 is the intensity of the X-ray photons impinging on the first PA slice of the CT data set derived from IPEM Report 78, path length is the length travelled by the beam in each PA slice (irrespective of the number of

Front face of voxels

Central axis of pencil beam is shown by the solid arrow

Figure 3. Pencil beam impinging on neighbouring voxels in a posteroanterior (PA) slice subsequent to the first.

voxels traversed) and LAC_{eff_sliceN} is the effective linear attenuation coefficient for slice N. Equation 2 is applied for each pencil beam impinging on the PA CT data for all energies present in the virtual X-ray spectrum. It should be noted that each DRR generation takes 45–90 min (on a computer with a modern processor).

Energy absorbed in CR phosphor

The X-ray energy absorbed by the layer of phosphor was calculated with

$$
A = \int_0^{E\max} E \Big[I(E) \Big\{ 1 - \exp\Big(\frac{-\mu_{en}(E)}{\rho} \rho x \Big) \Big\} \Big] dE \quad (3)
$$

where μ_{en}/ρ is the mass energy-absorption coefficient of the phosphor; ρx the mass loading of the phosphor (weight per unit area of phosphor; g cm^{-2}); $I(E)$ the photon spectrum incident on the CR phosphor (derived via Equation 2 for all pencil beams); and E the photon energy. The elemental composition of Agfa CR phosphor, BaSrFBrI:Eu was used to calculate μ_{en}/ρ for each photon energy using the XCOM database. The value of ρx used was 0.08 g cm^{-2} (personal communication, Mark O'Herlihy, Agfa, 2009). Increased photon absorption owing to the k-edges of iodine and barium (33.2 and 37.4 keV, respectively) were included in the calculation. All subsequent DRR images were calculated as energy absorbed by the CR phosphor. As discussed under ''DRR calculation'', each DRR is smaller than a real CR image. As such, the final DRR was resized (to match that of a CR image) using bicubic interpolation (the output pixel value is a weighted average of pixels in the nearest 4-by-4 neighbourhood). We tested the accuracy of image resizing by comparing SNRs and dynamic ranges of original and resized images. All SNRs (lung, spine and diaphragm) agreed to within 2%, minimum pixel values were always the same, and maximum pixel values agreed to within 3%. This is not surprising since no noise is contained in a raw DRR. Although this adds a systematic error, we felt it small enough to continue and see if it affected the subsequent validation results.
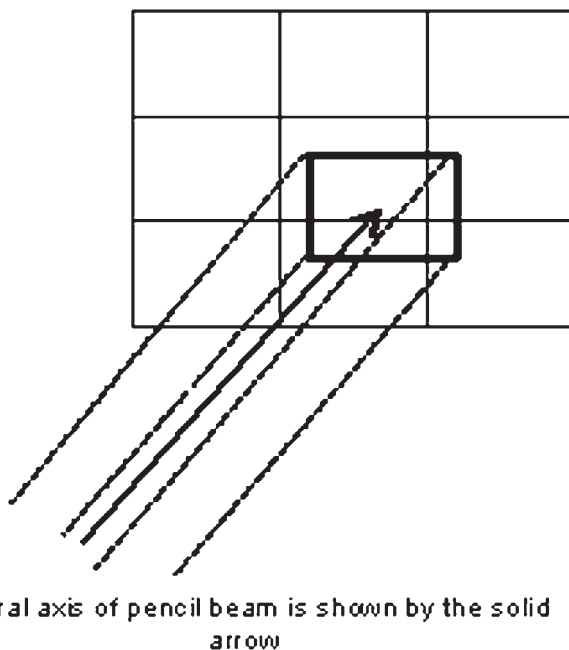
Linearisation of pixel value data

To measure scatter and scatter fractions (SFs), and add frequency-dependent noise to a DRR, images must be collected from the CR system. DRR images are displayed in terms of energy absorbed by the CR phosphor and are linear (DRR pixel values increase linearly with mAs). Because of this, images collected from the CR system must also be linear. However, CR systems are seldom linear, as is the case with the Agfa system used in this study. Pixel values of images acquired on the CR system were linearised by measuring the system transfer function (detector response). This was done by obtaining a series of six uniform open field exposures at each tube potential (50–150 kVp in steps of 10 kVp) covering an exposure range of approximately 1–15 µGy air kerma at the cassette measured with the cassette removed and replaced with a calibrated 6 cc ionisation chamber (Radcal Corporation, Monrovia, CA). Patient attenuation was approximated using 20 cm of polymethyl methacrylate (PMMA) at the tube port with a focus to cassette distance of 180 cm (PMMA used as a result of its similar X-ray absorption properties of water). For each tube potential used practically, the energy absorbed in the CR phosphor was calculated using the method described under ''Energy absorbed in CR phosphor'' (measurement of air kerma here was not used for calculation of energy absorbed in the phosphor, but to ensure exposure factors used were in the correct diagnostic energy range, *i.e.* 1–15 µGy). The relationships between pixel value and energy absorbed in the phosphor for each tube potential were used to linearise all images acquired on the CR system (*i.e.* pixel values were converted to energy absorbed by the CR phosphor).

Scatter measurement and addition to DRR

Scattered photons do not contain clinically useful information and degrade the image quality of chest radiographs by creating a non-uniform background that reduces image contrast. The scatter fraction (SF) is defined as the ratio of the intensity of scattered radiation to that of total (scattered plus primary) radiation recorded on the image. Niklason et al [38] and Floyd et al [39] measured average scatter fractions of 0.55, 0.81 and 0.91 in the lung, retrocardiac and mediastinum regions of chest radiographs, respectively. Scatter in chest radiography is therefore not negligible and must be present in images produced for optimisation.

Our DRR images do not compute any scatter from the CT data, and therefore it must be added post calculation. To do this we made measurements of scatter and SFs across the whole chest radiograph using an array of 224 lead beam stops, each of 6 mm in thickness and diameter, 25 mm apart from one another, suspended on a 1 mm thick PMMA sheet. Measurements were made for a range of diagnostic tube potentials (50–150 kVp in steps of 10 kVp), using the chest portion of RANDO with the lead stop array positioned in front of the phantom. Images were acquired on the Agfa CR system discussed under ''Practical methodology''. As primary X-radiation is absorbed by the lead stops, their shadows in a radiograph provide an estimate of scatter. An image of the beam stops with and without the phantom was acquired at each tube potential with a sufficient tube current–time product, mAs, to provide a lgM of 2.00 ± 0.05. Each image was

linearised in terms of energy absorbed by the CR phosphor and the mean pixel value in the shadow of each lead stop was calculated. Each mean pixel value is a measure of scatter (in terms of energy absorbed in the phosphor). Similarly, the total energy absorbed (primary + scatter) was measured in each image without the lead stops present. Scatter and SFs (all linear in terms of energy absorbed by CR phosphor) were subsequently measured at the position of each lead stop, and a 2D interpolation program written in Matlab (bicubic interpolation that fits a bicubic surface through existing data points) was used to calculate the values of scatter and SFs across the entire image. Since each DRR is already linear one can define the total energy absorbed by the CR phosphor as DRR$_{\text{total}}$ (as scatter does not exist in the simulator, energy absorbed in the CR phosphor from all pencil beams is not simply primary absorption, but total). The amount of primary absorption (DRR$_\text{P}$) can then be calculated by removing a portion of the signal from DRR$_{\text{total}}$ by applying linear SFs measured experimentally using the following equation

$$\mathrm{DRR_P = DRR_{total} \times (1 - SF)} \qquad (4)$$

Linear scatter (measured experimentally) can then be added to DRR$_\text{P}$. The following equation was used

$$\mathrm{DRR_{P+S} = DRR_P + scatter} \qquad (5)$$

where DRR$_{\text{P+S}}$ is the primary DRR with linear scatter (measured experimantally) added. Scatter and SF masks here have been derived with the RANDO phantom and so easily fit over raw DRR images of RANDO. However, although only average size males have been identified in this study (of which RANDO is modelled), anatomy differs slightly patient to patient and as such scatter and SF masks do not always fit accurately over raw patient DRRs. To overcome this, scatter and SF masks intended for patient DRRs were registered to them using the Matlab image registration function. This function uses a linear conformal transform which assumes the basic shapes of both images are the same (as in this case), but one image is distorted by some combination of translation, rotation and scaling. The registration methods available in Matlab have been validated by Goshtasby [40, 41].

Addition of frequency dependent noise

Noise was added to each DRR$_{\text{P+S}}$ using a slightly different method described by Bath et al [27]. They argue that an image simulating an original image but at a lower dose (dose of the simulated image, Dsim < original image), Im$_{\text{sim}}$, is given by Im$(x,y)_{\text{sim}}$ = Im$(x,y)_{\text{orig scaled down}}$ + Im$(x,y)_{\text{noise}}$, where Im$(x,y)_{\text{orig scaled down}}$ is the original linear image scaled down to the simulated dose (Dsim), and Im$(x,y)_{\text{noise}}$ is an image containing the noise which will result in the equality noise power spectrum (NPS) $(u,v)_{\text{Imsim}}$ = NPS$(u,v)_{\text{Dsim}}$. However, because the original image is not noise free, the 2D NPS of the noise image is given by

$$NPS(u,v)_{\mathrm{Im}noise} = NPS(u,v)_{Dsim} - NPS(u,v)_{Dorig}\left(\frac{Dsim}{Dorig}\right)^2 \quad (6)$$

Our work differs in that the original image contains no noise, as such the second term in Equation 6 becomes zero. Because of this, NPS$(u,v)_{\text{Imsim}}$ = NPS$(u,v)_{\text{Dsim}}$ suggesting

a uniform linear noise image acquired on the CR system at a given dose level (effectively Dsim) will contain the correct frequency dependence required. This method assumes that the noise power spectrum (NPS) is a sufficient descriptor of the noise and that detective quantum efficiency (DQE) is constant over the dose variations that exist within the image. However, CR systems tend to have a decreasing DQE with dose but Bath et al argue that their method is sufficient for doses used clinically. A series of uniform noise images were collected from the CR system using the same experimental set-up described under ''Linearisation of pixel value data''. Images were acquired at tube potentials 50–150 kVp in steps of 10 kVp across a range of clinically relevant mAs values. Each noise image was linearised and the DC signal (mean value) set to zero (the addition of the noise image must not alter the mean pixel value of the simulated image). As each DRR$_{P+S}$ is an inhomogeneous image, corrections to the uniform noise image must be made since the noise in the low dose areas of a CR image would in reality be lower than that in the high dose areas. To take these local dose variations into account, the following correction is applied to the uniform noise image:

$$\mathrm{Im\_}noise(x,y)_{corr} = \mathrm{Im\_}noise(x,y)_{unif} \sqrt{\frac{DRR_{P+S}}{PV_{mean}}} \quad (7)$$

where Im_noise$(x,y)_{corr}$ is the corrected noise image, Im_noise$(x,y)_{unif}$ is the uniform noise image, DRR$_{P+S}$ is the primary DRR with scatter added and PV$_{mean}$ is the mean pixel value of Im_noise$(x,y)_{unif}$. For the derivation of these this formula the reader should refer to Bath et al [27]. Each corrected noise image acquired with a given incident air kerma at the CR cassette was added to the DRR$_{P+S}$ corresponding to the same level of air kerma incident (7.0 ± 0.4 µGy at each tube potential for a lgM=2.00) at the CR cassette through the lung region of each DRR$_{P+S}$. This air kerma value was established using a pixel value to air kerma relationship derived previously for this CR system (*i.e.* the mean pixel value in the lung region was measured and converted to air kerma).

Phantom and patient image acquisition

To test and validate the DRR simulation, the chest portion of the RANDO phantom was scanned and reconstructed using the scan protocol and reconstruction parameters discussed in under ''CT data preparation''. CR images of the phantom were also acquired at tube potentials 50–150 kVp (in steps of 10 kVp) with a sufficient tube current–time product (mAs) to provide a lgM of 2.00 ± 0.05. Half and double mAs values were also used at each tube potential to assess the effects of dose reduction and escalation in the results of the computer model. All images were subsequently transferred to a separate computer. CT images are inherently of lower resolution than CR images. Therefore, one would expect the resulting DRR image to have a resolution inferior to that of a CR image. We felt it prudent to measure this quantitatively. As such, the MTF of a DRR image derived using a Teflon edge phantom was compared with the MTF of a CR image.

Further validation was performed with clinical images so local research ethics committee approval was obtained to allow the use of retrospective clinical CT and CR images. This study was concerned with optimising CR chest imaging for average size males, so image data of suitable patients (weight approximately 70 ± 10 kg identified by the expertise of the examining radiographer) were identified on the CT scanner and CR system. For the former, data were reconstructed as per the parameters discussed under ''CT data preparation'' prior to transfer to a separate computer. For the latter, beam quality, mAs and focus to detector distance used for their exposures were recorded. Images were transferred to a separate computer after Agfa-specific post-processing (MUSICA) was removed.

Results and discussion

CT data preparation

SNRs in the lung, spine and diaphragm regions of DRRs reconstructed without a noise removal filter, and with filters of size 7×7, 14×14 and 21×21, respectively, demonstrated <0.5% change. There was no difference in the dynamic range of the images. This demonstrates that quantum noise added to the resulting DRR images dominates over any noise present in the CT data. This is probably due to the averaging and summing process of X-ray pencil beam ray casting (averaging and summing causes all the voxels intersected by each pencil beam to tend to their true value). Because of the minimal effect on image quality in the resulting DRRs, no noise removal filter was applied to the CT data prior to DRR calculation.

DRR calculation

Figure 4a,b shows raw DRR images (no scatter or noise present) of the RANDO phantom reconstructed with tube voltages of 50 and 150 kVp respectively (matched lgM=2.00 ± 0.05). It can be seen in Figure 4a,b that contrast decreases as the tube voltage increases. This is because there is a decrease in differences between the linear attenuation coefficients of different human tissues with an increase in voltage, since the photoelectric cross-section varies with energy as approximately E^{-3}. In this way, the photoelectric effect plays a dominant role in producing subject contrast at diagnostic energies.

Linearisation of pixel value data

The relationship between energy absorbed by the CR phosphor and pixel value were all found to be logarithmic (log$_e$, all r^2 >0.9995) and demonstrated slight dependence on tube potential. To account for this all image data were linearised using the resulting equations for each tube potential.

Scatter measurement and addition to DRR

Images of the RANDO phantom with the beam stops and subsequent scatter fraction mask are shown in Figure 5a,b. SFs were derived at each tube potential investigated and ranged from 0.4–0.65 in the lung region, 0.7–0.8 in the mediastinum region and 0.8–0.85 in the heart region. As can be seen, the widest variation for SFs is in the lung, which is in general agreement with SFs measured by Floyd et al [42].
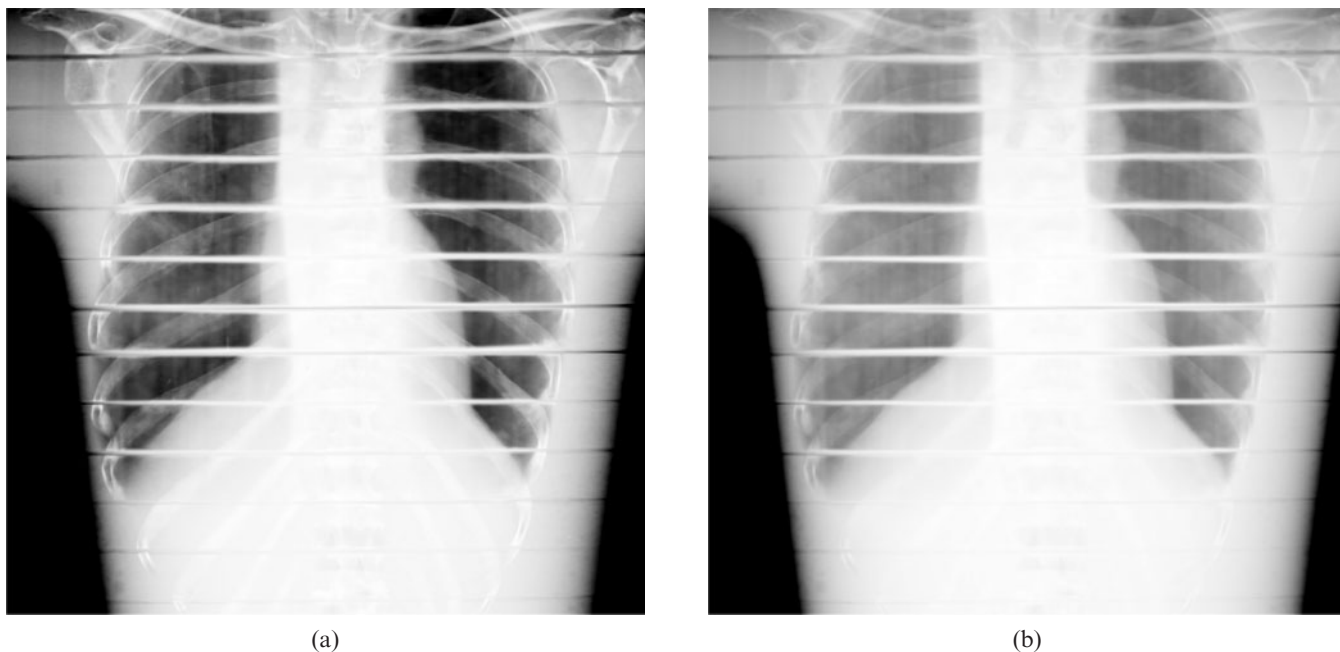
(a)

(b)

Figure 4. The RANDO phantom reconstructed (a) with a tube potential of 50 kVp, (b) with a tube potential of 150 kVp.

Addition of frequency-dependent noise

Figure 6 shows an example of a corrected noise image. The noise image in Figure 6 shows the effect of local dose variations. The added noise in the diaphragm and spine regions is lower than that in the lung regions. The noise in the lower dose regions would be overestimated (and underestimated in the higher dose regions) if no correction was applied.

Validation

Resolution of DRR compared with CR

The limiting spatial resolution of a DRR image measured from the MTF curve at the 2% level was 1.5 lp mm^{-1} and 0.6 lp mm^{-1} in the y and x directions respectively. This compares with 3 lp mm^{-1} for CR. Obviously, the resolution is poorer in the reconstructed
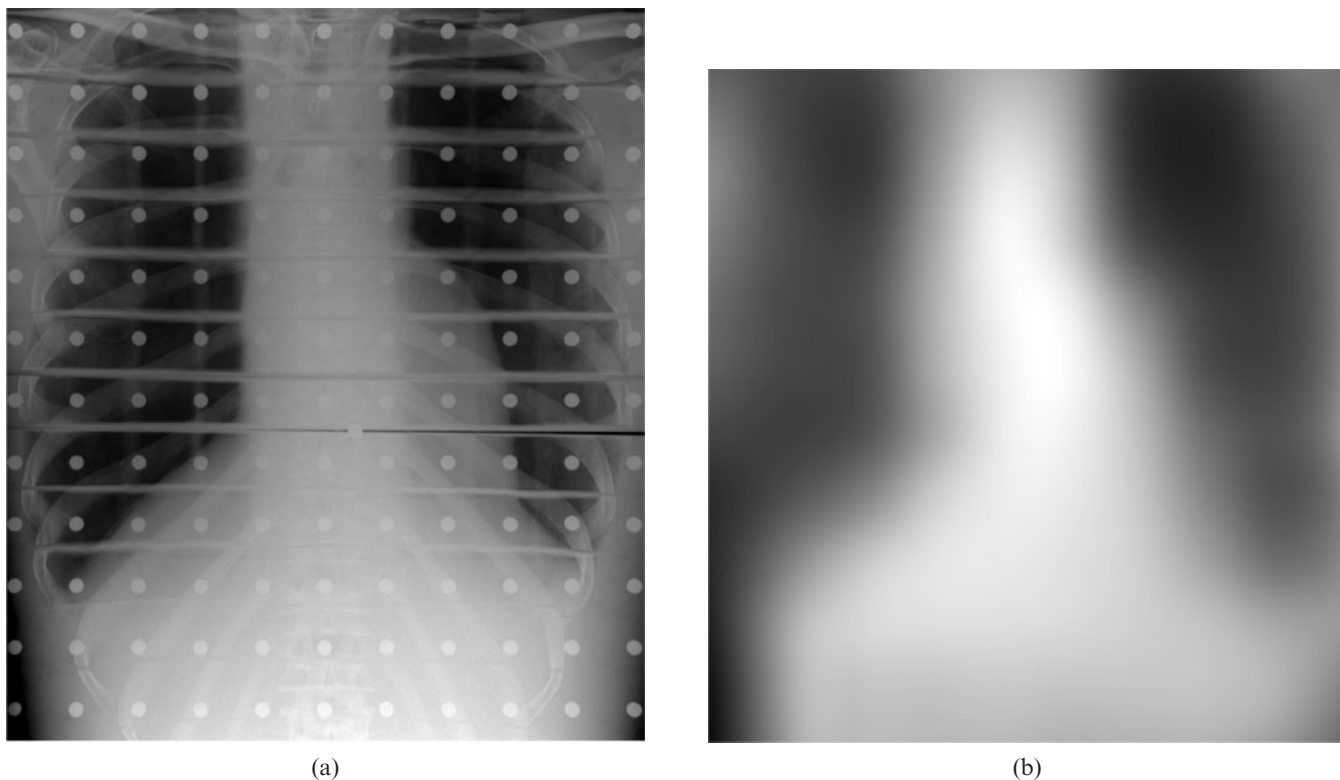

(a)

(b)

Figure 5. Radiograph of the RANDO phantom with (a) lead stops visible and (b) the resulting scatter mask.
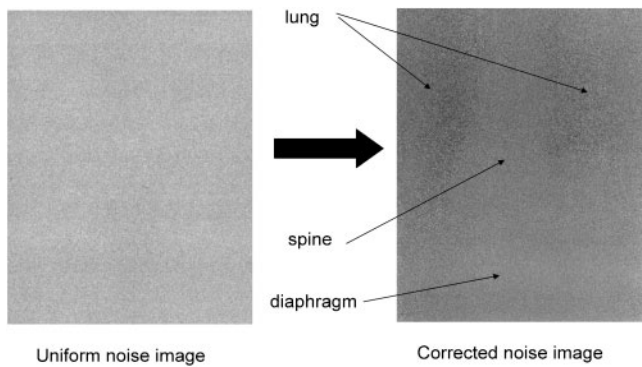
Figure 6. Corrected uniform linear noise image.

images; therefore, object information will always be presented at a lower resolution and a DRR image will never look exactly the same as a CR image of the same object. This may be a limiting factor (see ''Qualitative validation via expert evaluation'').

Validation with RANDO phantom

Initial validation was carried out with real CR and simulated DRR-generated images of the RANDO phantom. Figure 7a,b show a DRR (with scatter and noise added) and a real CR image of RANDO simulated and acquired at 60 kVp respectively. As can be seen in Figure 7a,b, both DRR images correlate visually with the real one. Quantitative validation was carried out by plotting histograms of pixel values and calculation of SNRs and tissue-to-rib ratios (TRRs). It is important to compare SNRs as the level of both signal and noise in a digital image affect the visualisation of pathology. The

TRR is a metric that calculates the mean region of interest (ROI) pixel value of soft tissue to that of rib. As ribs cover a large area of a chest radiograph and can interfere with the detection of soft tissue lesions, it is important that a good agreement should exist between calculated DRR and acquired CR images. SNRs were measured in the hilar, spine and diaphragm regions of each image using ROIs consisting of approximately 2500 (50×50) pixels. TRRs were measured in the lateral pulmonary region. As discussed under ''Methods and materials'', each raw DRR (no noise or scatter added) was resized to match that of a real CR image. The impact on signal and dynamic range in doing this was small ($<2\%$). As such, the resized DRR pixel area matches that of CR. Figure 8 compares real (CR) and simulated (DRR) histograms of pixel values acquired and reconstructed at a tube potential of 60 kVp, respectively. It can be seen in Figure 8 that the histogram produced from the simulated DRR image is very similar in shape to that produced from the real CR image (other tube potentials not shown but follow the same trend). However, the DRR histogram exhibits a reduced dynamic range relative to the CR histogram, possibly due to reasons discussed under ''Validation with clinical images''.

Figure 9a,b show histograms of real CR and simulated DRR images acquired and reconstructed with exposure factors 90 kVp, 1 and 4 mAs, respectively. Histograms produced from simulated images are similar shape to those produced from real CR images, and although their dynamic range is slightly smaller, they are shifted to the correct positions on the pixel value axis. This is encouraging, as it demonstrates the simulator correctly increases/decreases pixel values according to increased/decreased exposure to the detector, and as such can be
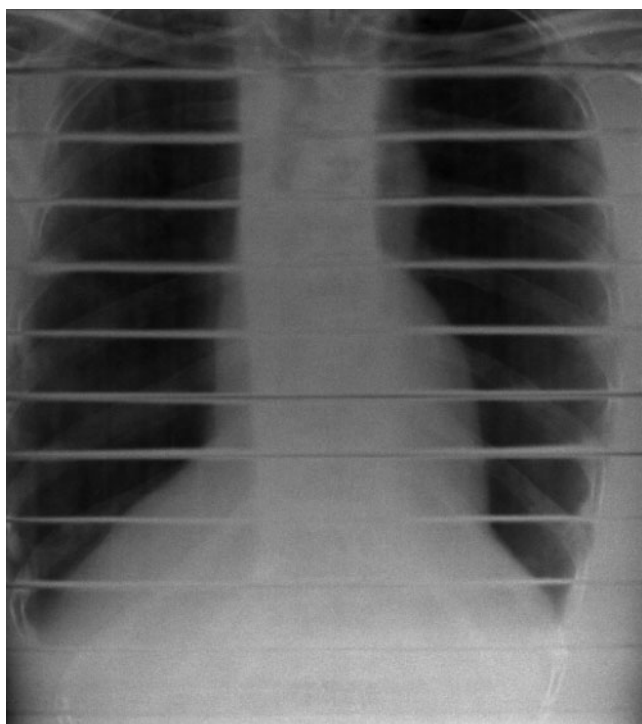
(a)
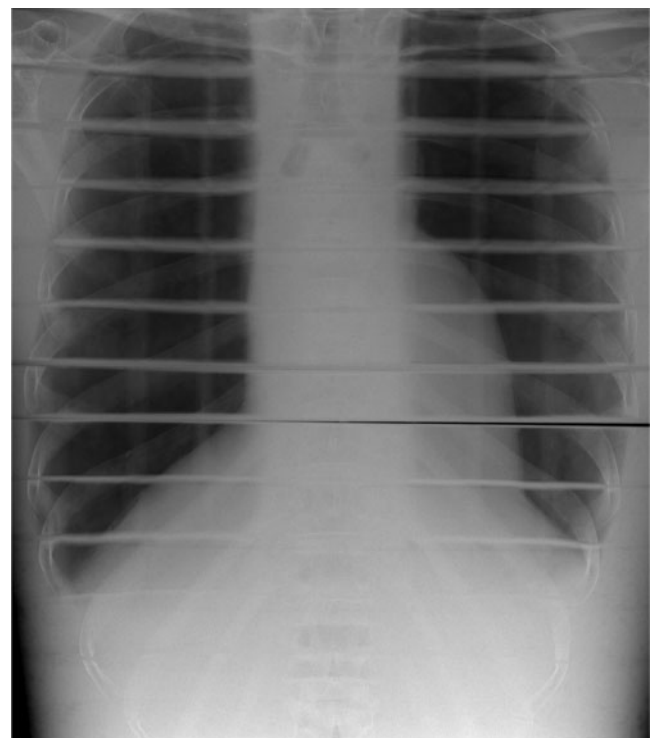
(b)

Figure 7. (a) Digitally reconstructed radiograph (with scatter and noise) of the RANDO phantom; (b) computed radiography image of the RANDO phantom.

CR - 60 kVp 10 mAs
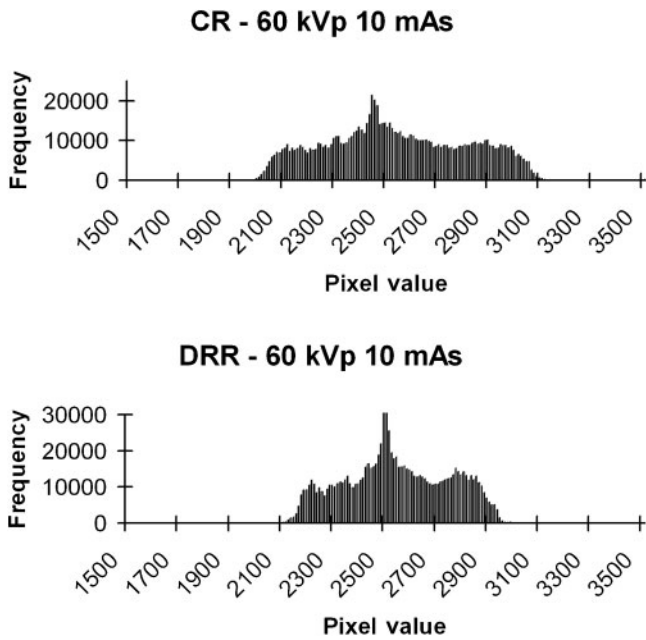

DRR - 60 kVp 10 mAs

Figure 8. (a) Computed radiography histogram of pixel values of the RANDO phantom at 60 kVp 10 mAs; (b) digitally reconstructed radiograph histogram of pixel values of the RANDO phantom at 60 kVp 10 mAs.

used for dose escalation/reduction studies, assuming levels of noise are also correct.

Table 4 compares SNRs of real CR images to that of DRR images in the lung, spine and diaphragm (matched lgM=2.00±0.05). It is clear from Table 4 that all DRR-calculated and CR-measured SNR values are in good agreement, the maximum deviation being 10% (mean= 5%). The addition of frequency-dependent noise does

have its limitations since NPS does not give a complete description of the noise properties of the system. However, this is often neglected because dose levels used clinically produce stochastic noise that dominates over structure noise. For a description of how the tolerances were estimated, the reader is referred to [16].

Table 5 shows the effect increasing and decreasing the dose has on subsequent SNR calculations and measurements with a tube potential of 90 kVp. Table 5 clearly shows a good agreement in SNRs measured in the CR and DRR images respectively. All other tube potentials tested produced similar results, and as such show that the model can reproduce images acquired with decreases/increases in dose.

Table 6 demonstrates TRRs calculated and measured in DRR and CR images, respectively. As seen in Table 6, all TRRs are in good agreement. The maximum difference in measured (CR) and calculated (DRR) is 1.3%. It can be seen that TRR decreases with increasing tube potential. This is due to the ribs attenuating a higher percentage of incident photons at lower potentials than soft tissue, thus forcing up the TRR.

Validation with clinical images

Validation with real patient data was carried out with 10 average male CR chest images all acquired with exposure factors 70 kVp, 5 mAs unless otherwise stated. Figure 10a,b compares an image of one of these males to that of a DRR-simulated image (both typical of their cohort). As with the RANDO images, the simulated DRR patient image correlates visually with the real one. The mean (±SD) of the minimum and maximum histogram values for 10 real CR images were 1690±280 and 3080±260, respectively. For 10 DRR images, these values

CR - 90 kVp 1 mAs

DRR - 90 kVp 1 mAs

(a)

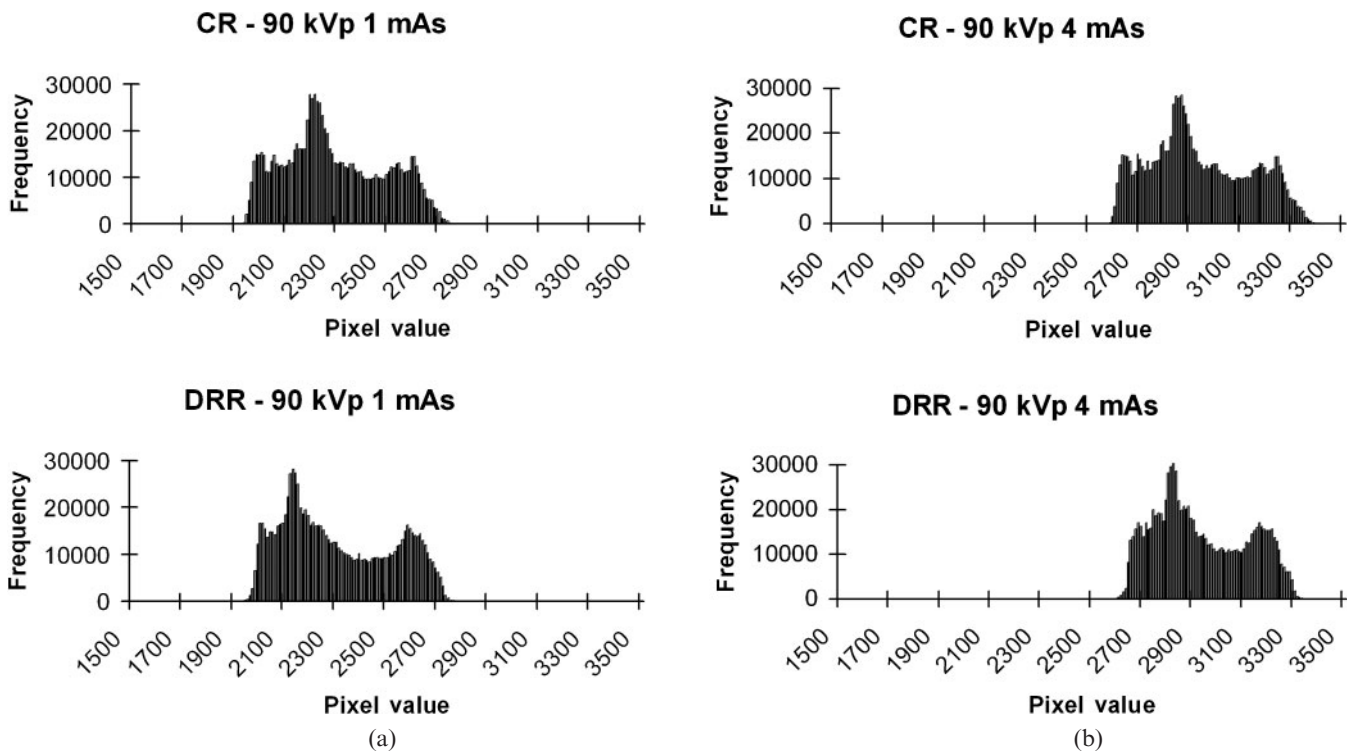## CR - 90 kVp 4 mAs

DRR - 90 kVp 4 mAs

(b)

Figure 9. Real computed radiography and simulated digitally reconstructed radiograph (DRR) histograms acquired and simulated with exposure factors 90 kVp, 1 (a) and 4 mAs (b), respectively.

Table 4. Comparison of signal-to-noise ratios (SNRs) measured in the lung, spine and diaphragm (diap) regions in digitally reconstructed radiograph (DRR) and real computed radiography (CR) images

RANDO SNR (all ± 30)						
Tube potential (kVp)	DRR lung	CR lung	DRR spine	CR spine	DRR diap	CR diap
50	200	195	104	108	82	78
60	199	199	112	112	83	81
70	194	208	115	108	92	87
80	192	194	92	95	72	76
90	215	208	125	124	105	103
100	214	208	126	117	94	98
110	214	221	138	137	103	109
120	204	210	115	118	100	99
130	203	199	118	111	81	88
140	199	209	120	119	89	88
150	203	202	94	97	89	90

Table 5. Comparison of signal-to-noise ratios (SNRs) measured in the lung, spine and diaphragm (diap) regions in digitally reconstructed radiograph (DRR) and real computed radiography (CR) images with varying mAs

	RANDO SNR (all ± 30)					
mAs	DRR lung	CR lung	DRR spine	CR spine	DRR diap	CR diap
1	179	185	119	115	90	91
2	215	208	125	124	105	103
4	266	263	130	128	116	119

were 1750 ± 270 and 2820 ± 290. The calculated (DRR) measure of dynamic range is smaller than that measured (CR). This is to be expected because although many tissue types have been modelled (using the RMI Gammex phantom), we are nevertheless limited to those contained within the phantom (Sandborg et al [20] reported similar findings with their Monte Carlo computer model). Also, the voxel size ($0.34 \times 0.34 \times 0.8$ mm) is probably larger than some of the smaller structures within the body. There is typically a slight shift of the histogram peak to the lower pixel values for CR images. This is probably due to slightly more scatter recorded in the images acquired with real patients because of the presence of more fat than the RANDO phantom.

Mean SNRs ($\pm$ SD) in the lung region of 10 real patient images and 10 simulated DRR images were 123.1 ± 18.8 and 124.1 ± 18.1, respectively. All images were chosen at random, since it was not possible to simulate a DRR image of a given patient and obtain a CR image of the same patient. Both mean values are the same given the standard deviations (SDs). The differences in SNRs are most likely due to differences in patient size (although they are "average", a weight range of 70 ± 10 kg was chosen) leading to changes in X-ray absorption and scatter. Mean ($\pm$ SD) DRR and CR SNR values for the spine region were 61.9 ± 7.6 and 60.3 ± 4.5. This again shows good similarity. Mean ($\pm$ SD) DRR and CR SNR values for the diaphragm region were 31.4 ± 2.0 and 24.7 ± 3.1. The mean SNR value for the diaphragm is lower in the real CR images than that of the simulated DRR images. This is probably due to more fat surrounding the abdomen of the patients relative to that of RANDO. This will increase the amount of scatter reaching the CR phosphor and hence noise, thus forcing down the SNR. However, image quality in the diaphragm is of limited importance in chest radiography [4], so this difference is likely to be of no significance.

This process was repeated for 10 average patient chest images acquired with 85 kVp and 4 mAs. Mean ($\pm$ SD) DRR and CR SNR values for the lung region were 104.0 ± 17.7 and 101.6 ± 19.2, respectively, for the spine 39.7 ± 4.7 and 44.7 ± 7.1, respectively, and for the diaphragm region 24.8 ± 2.4 and 22.8 ± 3.2, respectively.

As per the SNR measurements, 10 random real and simulated patients were used to measure the mean TRR. Mean ($\pm$ SD) DRR and CR TRR values were 1.071 ± 0.005 and 1.075 ± 0.004. The difference is probably due to varying rib thicknesses in the patients chosen. Nevertheless, there is a satisfactory agreement.

Qualitative validation via expert evaluation

4 independent experienced image evaluators (2 radiologists and 2 reporting radiographers) have seen a sample of 50 simulated images on calibrated PACS monitors and their opinions were very positive. All remarked that although image resolution was not as good as real radiographs, each contained sufficient clinical detail, were

Table 6. Comparison of tissue-to-rib ratios (TRRs) measured in digitally reconstructed radiograph (DRR) and real computed radiography (CR) images

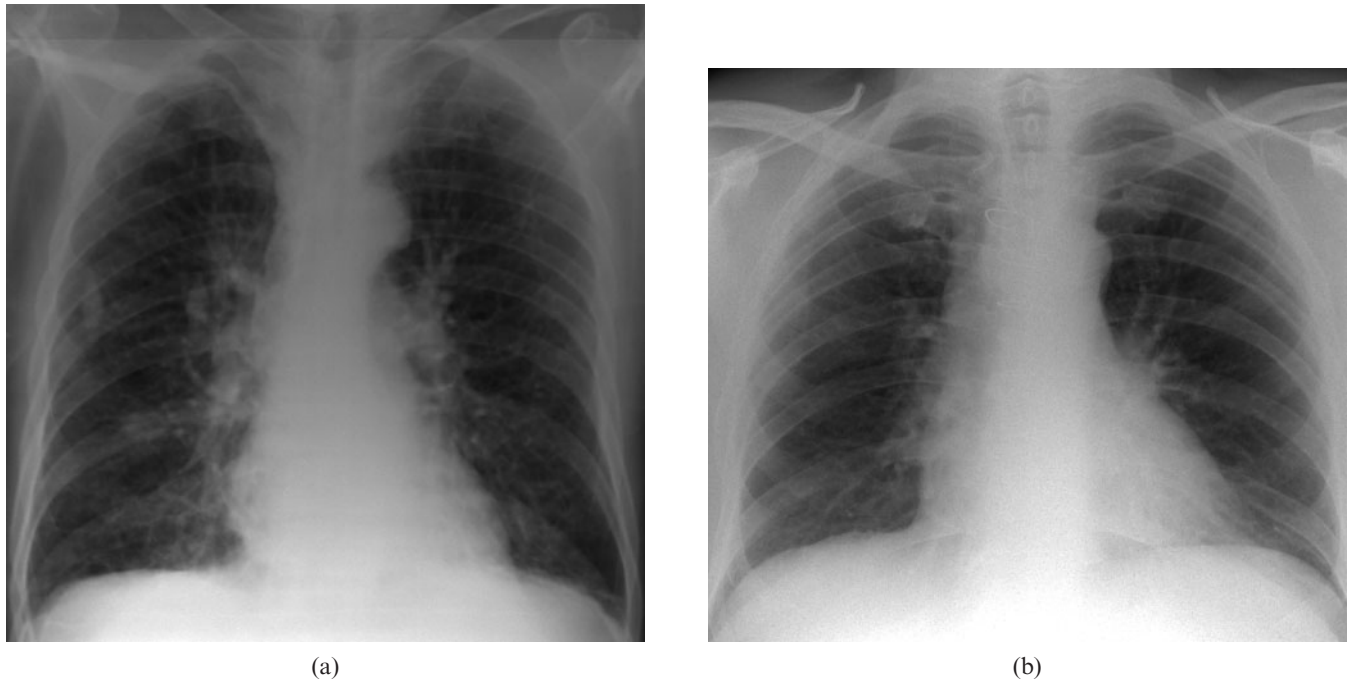| TRR RANDO (all ± 0.005)		
Tube potential (kVp)	TRR DRR	TRR CR
50	1.060	1.069
60	1.044	1.052
70	1.039	1.044
80	1.031	1.032
90	1.032	1.034
100	1.029	1.032
110	1.030	1.031
120	1.028	1.030
130	1.027	1.027
140	1.026	1.026
150	1.023	1.025

(a) (b)

Figure 10. Digitally reconstructed radiograph (DRR) (with noise and scatter) of a real patient (a), and computed radiography image of a real patient (b). The DRR image was reconstructed using the following exposure factors: 75 kVp, 5 mAs and 180 cm focus to detector distance (FDD). The real image was acquired with the same factors. It should be noted that Figures 10a and b are not of the same patient. However, both are ''average'' height and weight (70 kg $\pm$ 10 kg).

definitely representative of chest anatomy and suitable for optimisation studies requiring anatomical noise.

Limitations of the simulation system

There are numerous limitations to this system. We believe the ones of most relevance are noise addition (due to DQE dependency with dose variations in an image) and poorer inherent resolution of CT data than that of CR images (although still much better than voxelated phantoms used in Monte Carlo studies). This has led to DRR images exhibiting lower resolution than desired. This problem will not be an issue in future if CT scan resolution improves and approaches that of CR. However, the prime objective of this work was to develop a simulation system that produces chest images adequately simulating anatomical noise and features. Radiologist comments are favourable, so spatial resolution of these DRR images is not a limiting factor.

Conclusions and future work

Our DRR calculator scheme provides a realistic model of the Agfa CR digital imaging system for chest radiography (of average size males). Anatomical noise is adequately simulated using human chest CT data sets. Scatter and system noise have been successfully added post-DRR calculation, resulting in SNRs, TRRs and pixel value histograms that are in good agreement with those measured in CR-acquired images. Although DRR resolution is not as good as real CR images, four independent expert image evaluators believe DRR images adequately simulate real radiographs and provide realistic anatomical features. Therefore, this computer model provides us with

a tool that can be used by radiologists to grade quality for images derived with different X-ray system parameters, without the need to perform repeat exposures on patients. We intend to use it for optimisation of clinical chest imaging with this Agfa CR system. The simulator can be adapted to include other digital detector technologies if X-ray photon absorption, noise and scatter properties of the system in question are measured and incorporated into the simulation.

Future work will include adding pathology (and validating) to the CT data to simulate lesions in the resulting DRR, modelling antiscatter grids and air-gap techniques for scatter reduction investigations, and simulating large/obese patients.

Acknowledgments

References

1. Bochud FO, Valley JF, Verdun FR, Hessler C, Schnyder P. Estimation of the noisy component of anatomical backgrounds. Med Phys 1999;26:1365–70.
2. Samei E, Flynn MJ, Eyler WR. Detection of subtle lung nodules: relative influence of quantum and anatomical noise on chest radiographs. Radiology 1999;213:727–34.
3. Samei E, Eyler W, Baron L. Effects of anatomical structure on signal detection. In: Kundel JHL and Van Metter RL, editors. Handbook of medical imaging. Vol. 1. Physics and Psychophysics. Beutel, Orlando, FL 2000:655–82.

4. Keelan BW, Topfer K, Yorkston J, Sehnert WJ, Ellinwood JS. Relative impact of detector noise and anatomical structure on lung nodule detection. Proc SPIE 2004;5372:230–41.

5. Sund P, Bath M, Kheddache S, Mansson LG. Comparison of visual grading analysis and determination of detective quantum efficiency for evaluation system performance in digital chest radiography. Eur Radiol 2004;14:48–58.

6. Hakansson M, Bath M, Borjesson S, Kheddache S, Allansdotter J, Mansson LG. Nodule detection in digital chest radiography: effect of system noise. Radiat Prot Dosim 2005;114:97–101.

7. Hakansson M, Bath M, Borjesson S, Kheddache S, Grahn A, Ruschin M, et al. Nodule detection in digital chest radiography: summary of the RADIUS chest trial. Radiat Prot Dosim 2005;114:114–20.

8. Bath M, Hakansson M, Borjesson S, Kheddache S, Grahn A, Bochud FO, et al. Nodule detection in digital chest radiography: introduction to the RADIUS chest trial. Radiat Prot. Dosim 2005;114:85–91.

9. Bath M, Hakansson M, Borjesson S, Kheddache S, Grahn A, Bochud FO, et al. Nodule detection in digital chest radiography: part of image background acting as pure noise. Radiat Prot Dosim 2005;114:102–8.

10. Bath M, Hakansson M, Borjesson S, Hoeschen C, Tischenko O, Kheddache S, et al. Nodule detection in digital chest radiography: effect of anatomical noise. Radiat Prot Dosim 2005;114:109–13.

11. Dobbins JT, Rice JJ, Beam CA, Ravin CE. Threshold perception performance with computed radiography: implications for chest radiography. Radiology 1992;183:179–87.

12. Chotas HG, Floyd CE, Dobbins JT, Ravin CE. Digital chest radiography with photostimulable phosphors: signal-to-noise ratio as a function if kilovoltage with matched exposure risk. Radiology 1993;186:395–8.

13. Nobuhiro O, Hajime N, Seiichi M, Kunihiro T, Katsumi N, Akira Y. Optimal beam quality for chest radiography. Invest Radiol 1996;31:126–31.

14. Tingberg A, Sjostrom D. Search for optimal tube voltage for image plate radiography. Invest Radiol 1996;31:126–31.

15. Honey ID, MacKenzie A, Evans DS. Investigation of optimum energies for chest imaging using film-screen and computed radiography. Br J Radiol 2005;78:422–7.

16. Moore CS, Liney GP, Beavis AW, Saunderson JR. A method to optimize the processing algorithm of a computed radiography system for chest radiography. Br J Radiol 2007;80:727–30.

17. Moore CS, Beavis AW, Saunderson JR. Investigation of optimum X-ray beam tube voltage and filtration for chest radiography with a computed radiography system. Br J Radiol 2008;81:771–7.

18. Moore CS, Beavis AW, Saunderson JR. Investigating the exposure class of a computed radiography system for optimisation of physical image quality for chest radiography. Br J Radiol 2009;82:705–10.

19. Launders JH, Cowen AR, Bury RF, Hawkridge P. Towards image quality, beam energy and effective dose optimisation in digital thoracic radiography. Eur Radiol 2001;11:870–5.

20. Sandborg M, McVey G, Dance DR, Persliden J, Alm Carlsson G. A voxel phantom based Monte Carlo computer program for optimisation of chest and lumber spine x ray imaging systems. Radiat Prot Dosim 2000;90:105–8.

21. Sandborg M, McVey G, Dance DR, Alm Carlsson G. Schemes for the optimization of chest radiography using a computer model of the patient and X-ray system. Med Phys 2001;28:2007–19.

22. Sandborg M, Tingberg A, Ullman G, Dance DR, Alm Carlsson G. Comparison of clinical and physical measures of image quality in chest and pelvis computed radiography at different tube voltages. Med Phys 2006;334:169–75.

23. Ullman G, Sandborg S, Dance DR, Hunt RA, Carlsson GA. Towards optimization in digital chest radiography using Monte Carlo modelling. Phys Med Biol 2006;51:2729–43.

24. Zubal G, Harrell CR, Smith EO, Rattner Z, Gindi G, Hoffer PB. Computerized three-dimensional segmented human anatomy. Med Phys 1994;21:299–302.

25. ICRP. The 2007 Recommendations of the International Commission on Radiological Protection. 2007 ICRP Publication 103. Oxford, UK: Pergamon.

26. Bath M, Hakansson M, Hansson J, Mansson LG. A conceptual optimization strategy for radiography in a digital environment. Radiat Prot Dosim 2005;114:230–5.

27. Bath M, Hakansson M, Tingberg A, Mansson LG. Method of simulating dose reduction for digital radiographic systems. Radiat Prot Dosim 2005;114:253–9.

28. Milickovic N, Baltas D, Giannouli S, Lahanas M, Zamboglou N. CT imaging based digitally reconstructed radiographs and their application in brachytherapy. Phys Med Biol 2000;45:2787–800.

29. Cai W, Sakas G. DRR volume rendering using splatting in shear-warp context. Nuclear Sci Procs IEEE 2001;3:12–17.

30. Westover LA. Interactive volume rendering. In: Proceedings of Volume Visualisation Workshop, Chapel Hill, NC, 18–19 May 1989, Department of Computer Science, University of North Carolina, Chapel Hill, NC, 1989: 9–16.

31. Cranley BJ, Gilmore GWA, Fogarty A, Desponds L, Sutton DG. Catalogue of diagnostic X-ray spectra & other data. IPEM Report 78 (CD-ROM). York: IPEM, 1997.

32. Shrimpton PC, Wall BF, Fisher ES. The tissue-equivalence of the Alderson-Rando anthropomorphic phantom for X-rays of diagnostic qualities. Phys Med Biol 1981;26:133–9.

33. Roberts JA, Evans SC, Rees M. Optimisation of imaging technique using direct digital radiography. J Radiol Prot 2006;26:287–99.

34. Hilts M, Duzenli C. Image filtering for improved dose resolution in CT polymer gel dosimetry. Med Phys 2004;31:39–49.

35. Higgins PD, Attix FH, Hubbell JH, Seltzer SM, Berger MJ, Sibata CH. Mass energy transfer and mass energy absorption coefficients, including in flight positron annihilation for photon energies 1 keV to 100 MeV. National Institute of Standards and Technology, NISTIR 4680. Gaithersburg, MD: US Department of Commerce, 1992.

36. Siddon RL. Fast calculation of the exact radiological path for a three-dimensional CT array. Med Phys 1985;12:252–255.

37. Swan E II, Mueller K, Möller T, Shareef N, Crawfis Rayagel R. An anti-aliasing technique for splatting. In: Proceedings of IEEE Conference on Visualization 1997. 1997: 197–204.

38. Niklason LT, Sorenson JA, Nelson JA. Scattered radiation in chest radiography. Med Phys 1981;8:677–81.

39. Floyd CE, Lo JY, Chotas HG, Ravin CE. Quantitative scatter measurement in digital radiography using a photo-stimulable phosphor imaging system. Med Phys 1991;18:408–13.

40. Goshtasby A. Piecewise linear mapping functions for image registration. Pattern Recognit 1986;19:459–66.

41. Goshtasby A. Image registration by local approximation methods. Image Vis Comput 1988;6:255–61.

42. Floyd CE, Baker JA, Lo JY, Ravin CE. Measurement of scatter fractions in clinical bedside radiography. Radiology 1992;183:857–61.